The International Journal of Advanced Manufacturing Technology (2023) 126:3023–3038
https://doi.org/10.1007/s00170-023-11288-2

ORIGINAL ARTICLE

Laser-directed energy deposition of CoCrFeNiTi high entropy alloy coatings: effects of powder geometry and laser power

Yunze Li[1] · Dongzhe Zhang[1] · Yingbin Hu[2] · Weilong Cong[1]

Received: 16 January 2023 / Accepted: 16 March 2023 / Published online: 27 March 2023

Abstract
CoCrFeNiTi high entropy alloy (HEA) has been extensively studied to serve as coating materials on complexly shaped parts of equipment used in industries such as oil, gas, and mining due to its high hardness, excellent wear resistance, and good high-temperature stability. Laser-directed energy deposition has potential to fabricated HEA caotings due to its advantages of excellent metallurgical bonding, high coating density, suppressed element segregation, and the capability of thick coating deposition. However, limited investigations have been conducted on the effects of input parameters (such as powder geometry and laser power) on the mechanical properties of laser DED fabricated CoCrFeNiTi high-entropy alloy coatings. In this study, CoCrFeNiTi HEA coatings have been fabricated on Ti substrates from spherical-shaped and irregular-shaped powders under different levels of laser power. The effects of powder geometry and laser power on molten pool thermal characteristics (including temperature, cooling rate, and solidification time), phase constitution, microstructure, and mechanical properties of hardness and wear resistance have been investigated. Under the same laser power, the utilization of irregular-shaped powders resulted in uniform microstructures and higher hardness. For the coatings fabricated from spherical-shaped powders, the increase of laser power could improve the microhardness and wear resistance. For the coatings fabricated from spherical-shaped powders, the increase of laser power could increase the microhardness. However, the wear resistance is increased and then decreased due to the increase in friction of coefficient.

Keywords High entropy alloys · CoCrFeNiTi · Coatings · Laser-directed energy deposition · Powder geometry · Laser power

1 Introduction

High entropy alloys (HEAs) are defined as the alloys containing more than five major elements of equal or nearly equal molar ratio with a mixing entropy generally greater than 1.5R (where R represents the gas constant 8.314 J/(K·mol)) and a simple solid solution structure (essentially FCC or BCC phases) [1–4]. Depending on element composition, HEAs can possess varieties of special properties, such as high hardness, outstanding wear resistance, good high-temperature strength, ferromagnetic, or excellent superconductivity [2, 4]. Among them, high hardness and high wear resistance are the most important properties needed for coating materials. It has been reported that the HEAs such as CoCrFeNiTi, CoCrFeNiAl, CoCrFeNiV, and FeCoNiAlB have extremely high microhardness (over 600 HV) and excellent wear resistance, which have the potential to serve as coating materials [5–7]. Compared with other high hardness HEAs, CoCrFeNiTi has the unique advantage of better compatibility with Ti due to the presence of Ti element. Ti and its alloys are the most widely used material in the oil, gas, and mining industries. Therefore, CoCrFeNiTi has a great development prospect in the future.

HEA coating deposition technologies including vacuum arc melting technique, plasma spray technique, solid-state cold spraying, laser-directed energy depositions (DED) technique, etc. [8–13]. Vacuum arc melting technique as the most commonly used method in HEA coatings fabrication has the disadvantages of segregation problem and cost limit. Plasma spray technique is an alternative method for

✉ Weilong Cong
weilong.cong@ttu.edu

1 Department of Industrial, Manufacturing, and Systems Engineering, Texas Tech University, Lubbock, TX 79409, USA

2 Mechanical and Manufacturing Engineering Department, Miami University, Oxford, OH 45056, USA

HEA coatings fabrication [14, 15]. However, during the plasma spray process, the coatings are mainly formed by the stacking and collision of semi-melted powders, leading to relatively low density and bonding quality [14]. The solid-state cold spraying is hard to spray hard brittle materials without using ductile binders [16]. Compared with these coating technologies, laser DED has advantages including the capability of complex and selective area coating, the capability of part remanufacturing, high density, small substrate deformation, and high-quality metallurgical bonding between coatings and substrates [17, 18]. In addition, the high cooling rate in laser DED can lead to non-equilibrium solidification, which helps to avoid component segregation and improves solid solution strengthening effects.

Recently, there are several investigations on the deposition of CoCrFeNiTi HEA coatings on Ti substrates by laser DED process [8, 9, 11, 19–23]. Most studies up to now focus on controlling their microstructures and further improving the mechanical properties by adjusting the elemental composition of HEA feedstock material powders. Tadashi et al. and Zhang et al. investigated the mechanical and corrosion properties of CoCrFeNiTi HEAs and found that the CoCrFeNiTi HEAs showed higher tensile strength and pitting corrosion resistance than conventional high corrosion resistant alloys including stainless steel and Inconel series Ni-based alloys [21, 23]. Shun et al. investigated the effects of Ti content on the mechanical properties of CoCrFeNiTi HEA [24]. Results show that with the increase of Ti content, the tensile strength and hardness were significantly increased. In most of the existing investigations, conventional spherical-shaped powders suitable for the laser additive manufacturing process were used to fabricate CoCrFeNiTi HEA coatings/parts [22, 23, 25]. It was also noted that in some other existing investigations, a mixture of spherical-shaped and irregular-shaped powders was used to fabricate CoCrFeNiTi HEA coatings/parts. The possible reason for using irregular-shaped powders was to promote the fully melting of the metal powders with high melting points [26, 27]. However, current investigations on the fabrication of CoCrFeNiTi HEA coatings/parts focused on the effects of element contents on the coating quality. The fabricated CoCrFeNiTi HEA coatings/parts had different elemental ratios. Comparing the results of the existing investigations, it was not possible to conclude that the powder geometry could significantly affect the hardness and wear resistance of CoCrFeNiTi HEA coatings/parts. It is necessary to confirm and further explain the effects of powder shape and laser power on the quality of CoCrFeNiTi HEA coating/parts by analyzing the changes of molten pool thermal characterizations, especially when controlling other variables (such as element ratio of feedstock powder, scanning speed, and powder feed rate).

In this study, CoCrFeNiTi HEA coatings were successfully deposited on Ti substrates using spherical-shaped and irregular-shaped powders by laser DED process under different levels of laser power. By using a high-resolution IR camera, the real-time dynamic molten pool temperature was measured and the cooling rate was further calculated. The effects of powder geometry and laser power on the molten pool temperature, cooling rate, and solidification time were investigated. Then, the effects of molten pool thermal characterizations on phase constitutions, microstructures, and mechanical properties of hardness and wear resistance of laser DED fabricated CoCrFeNiTi HEA coatings were further investigated.

2 Experiment procedures

2.1 Materials and powder treatment

As shown in Fig. 1, the pure spherical-shaped Co powder (99.9% purity), Cr powder (99.9% purity), Fe powder (99.9% purity), Ni powder (99.9% purity), and Ti powder (99.7% purity), (Atlantic Equipment Engineers Inc., NJ, USA) with the average particle size of 45 μm were used to prepare the spherical-shaped feedstock powder. For the irregular-shaped feedstock powder, the spherical-shaped Cr and Ti powders were replaced by the pure irregular-shaped Cr powder (99.9% purity) (Heeger Materials Inc., CO, USA) and Ti powder (99.9% purity) (Atlantic Equipment Engineers Inc., NJ, USA) with the smaller particle size of 15–45 μm. The reason for changing the powder geometry of Cr and Ti was that they have higher melting points (1907 °C and 1668 °C, respectively) than Ni (1455 °C), Co (1495 °C), and Fe (1538 °C). Their high melting point may lead to partially melting and reduce the fluidity of the liquid material in the melt pool. By using the irregular-shaped powders with smaller particle sizes, the laser refractive index would be reduced and the laser absorption capacity would be increased, thus promoting the fully melting of Cr and Ti powders with high melting points. The fully melting of material powders would have significant effects on the thermal characterization of the molten pool and influence the phase constitutions, microstructures, and mechanical properties of the CoCrFeNiTi HEA coatings. For both spherical-shaped and irregular-shaped feedstock powders, the atomic ratio of Co, Cr, Fe, Ni, and Ti powders was 1:1:1:1:1.

A planetary ball milling machine (ND2L, Torrey Hills Technologies LLC., USA) was used to mix and pretreat the feedstock powders in the air atmosphere for four hours. During the ball milling processes, the sun wheel and the milling jars rotated in opposite directions with a speed of 200 rpm. The weight ratio between powder and milling balls was 1:1. After the ball milling process, pure metal powders were uniformly mixed without significant changes in shape and size.

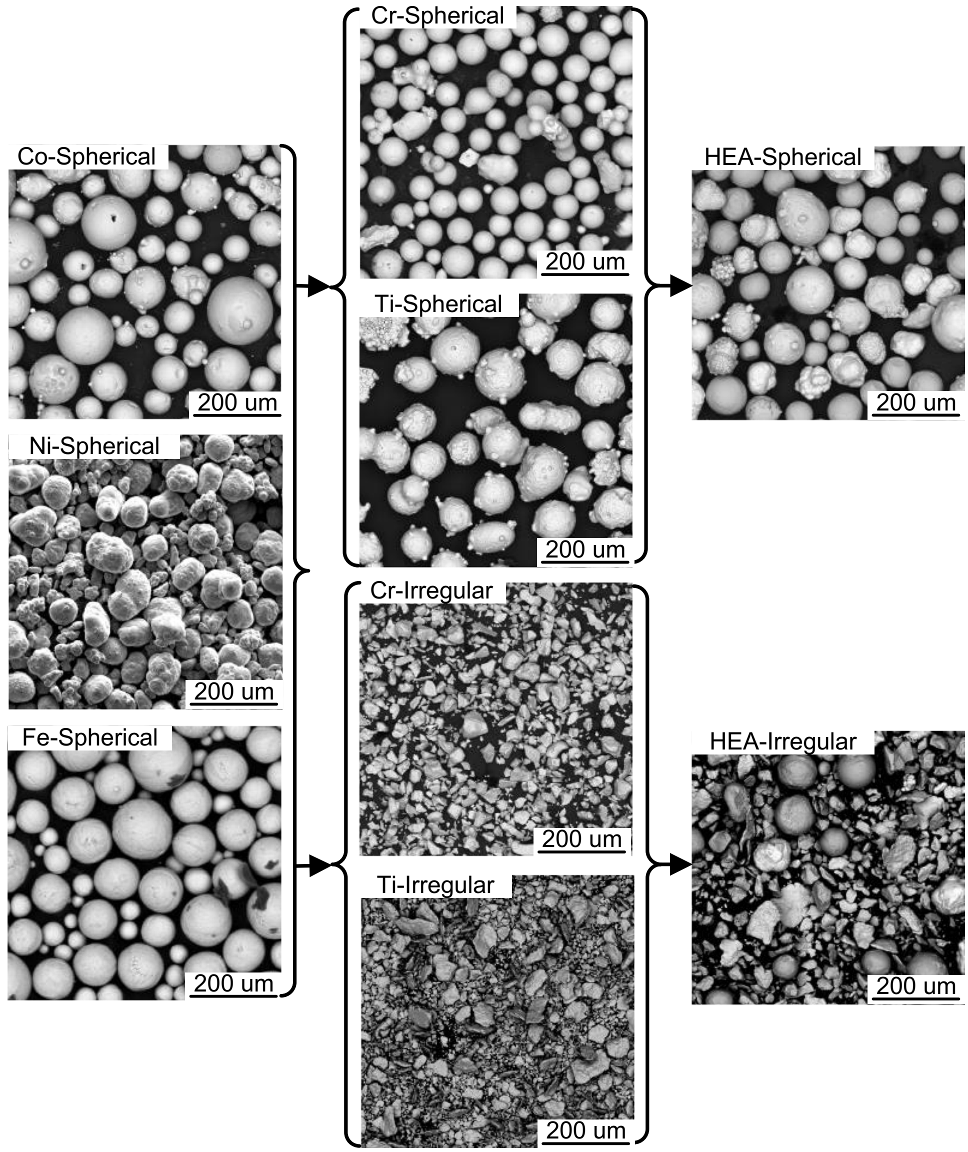

Fig. 1 SEM images of powder materials

2.2 Experiment setup

As shown in Fig. 2, a laser-engineered net shaping (LENS) system (450, Optomec Inc., USA) was used to conduct the experiments. To avoid the reactions between metal powders and oxygen, the sealed chamber was purged by argon gas to a low oxygen level (< 50 ppm) before the fabrication. During the fabrication, the feedstock powders were delivered by the argon gas stream. At the same time, a laser beam with a constant wavelength of 1064 nm was generated and transformed to the surface of Ti substrate, generating a molten pool and then catching the powders. When the laser beam moved away, the melted material powders in the molten pool solidified rapidly and generate the first deposited layer. When the laser beam finished the first layer tracking paths complying with the designed computer model, the deposition head moved up a distance of Z-axis increment. Then, the second layer was fabricated on top of the first layer. By repeating this procedure, the coatings were fabricated layer by layer. The dimensions of the fabricated coatings were 6 mm × 6 mm × 3 layers. To reduce the experimental errors, three samples were fabricated under each level of laser power using spherical-shaped and irregular-shaped feedstock powders, respectively. The detailed input parameters were listed in Table 1.

In order to investigate the effects of powder shape and laser power on molten pool characterizations, the one-layer single-track CoCrFeNiTi HEA coatings were also deposited in the consistent direction (x-direction), aiming at reducing the influence of adjacent tracks on temperature measurements. During the fabrication of single-track CoCrFeNiTi HEA coatings, a high-resolution infrared thermal camera (PYROVIEW 768 N, DIAS Inc., Dresden, Germany) was used to measure the molten pool temperature and the molten

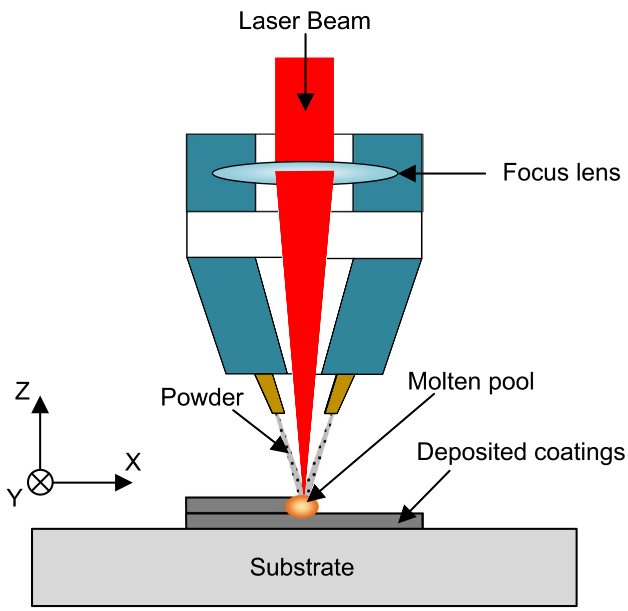

Fig. 2 Illustration on experimental setup

Table 1 Laser DED parameters of CoCrFeNiTi HEA coatings

Input fabrication variables	Values
Laser power (W)	250, 300, and 350
Beam diameter of laser (μm)	400
Wavelength of laser (nm)	1064
Deposit head scanning speed (mm/min)	254
Hatch distance (μm)	340
Layer thickness (μm)	432
Powder feeding rate (g/min)	3.5
Number of layers	3
Argon gas flow rate (L/min)	6

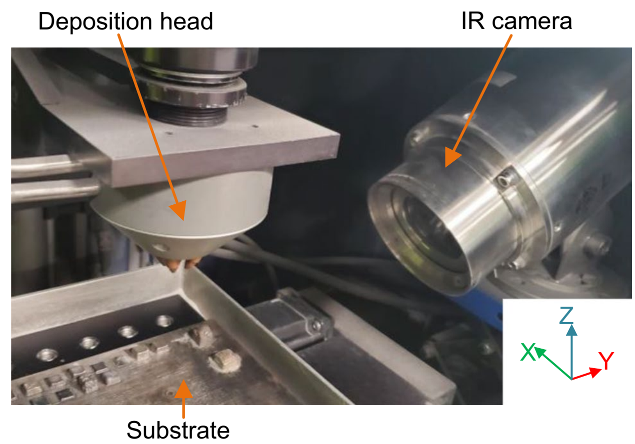

Fig. 3 IR camera setup

pool size with the sample rate of 25 Hz. As shown in Fig. 3, the infrared thermal camera was fixed inside the chamber, which is perpendicular to the direction of the laser deposition path. The angle between the thermal camera and substrate was 60°. The distance between the thermal camera and the molten pool was fitted as 20 cm. The professional software (PYROSOFT 3.22, DIAS Inc., Dresden, Germany) was used to colorize the image to analyze the real-time temperature.

2.3 Measurement procedures

In order to observe the microstructure and detect the microhardness and wear resistance, the fabricated coatings were ground and polished by a grinder-polisher machine (MetaServ 250 single grinder machine, Buehler, USA). The X-ray diffraction (XRD) machine (Ultima III, Rigaku Corp., The Woodlands, TX, USA) was used to analyze the phase constitutions. The samples were scanned from 20 to 80 degrees (2θ) with the scanning step of 0.02 degrees (2θ). The phases were fitted by the MDI/JADE software (Version 2020, Materials Data, Livermore, CA, USA). The scanning electron microscopy (SEM) equipped with a backscatter electron detector (BSD) system was used to observe the microstructure of the cross-sectional surface of the fabricated coatings. The energy dispersive X-ray spectroscopy (EDS) system was utilized to detect the element compositions.

The microhardness of the deposited coating layers was tested by a Vickers microhardness tester (Phase II, Upper Saddle River, NJ, USA) using a 10 N normal load with 10 s dwell time. Three samples were tested to measure the microhardness. The microhardness was measured five times for each of the three samples fabricated under each combination of input parameters. The average values and standard deviation of microhardness were reported. The wear rate was tested and measured by dry sliding tests at room temperature using a mechanical testing system (PB1000, Nanovea, Manufacturer in Irvine, CA, USA). The dry sliding tests were conducted three times for each of the three samples fabricated under each combination of input parameters. During the dry sliding test, a 1 mm radium SiC ball was sliding on the surface of the coating for 0.25 h with a load of 2 N, a constant sliding speed of 3 mm/s, and a sliding distance of 3 mm. After dry sliding, the scratching width was measured by an optical microscope (DSX-510, OLYMPUS, Tokyo, Japan). Wear volume lost V was calculated by Eq. 1 [23].

$$V = L \times \left[\frac{\pi R^2}{180} \times arcsin\left(\frac{W}{2R} \right) - \frac{W}{2} \times \sqrt{R^2 - \left(\frac{W}{2} \right)^2} \right] \quad (1)$$

where L was the sliding distance, mm; R was the radius of SiC ball, mm; W was the scratching width, mm. The wear rate W_r was calculated by Eq. 2.

$$W_r = \frac{V}{F(vT)} \tag{2}$$

where F was the load, N; v was the sliding speed, mm/s; T was the duration time, s.

2.4 Molten pool characterization analysis

A typical thermal image of the molten pool temperature for the one-layer single-track CoCrFeNiTi HEA coatings is shown in Fig. 4(a). It could be seen that the molten pools have an oval shape. The temperature along the cursor line from the left edge of the thermal image to the center of the molten pool is shown in Fig. 4(b). The maximum temperature was found at the center of the molten pool. The average value of the maximum temperature at each moment during the deposition process would be used to study the effects of powder geometry and laser power on the molten pool temperature.

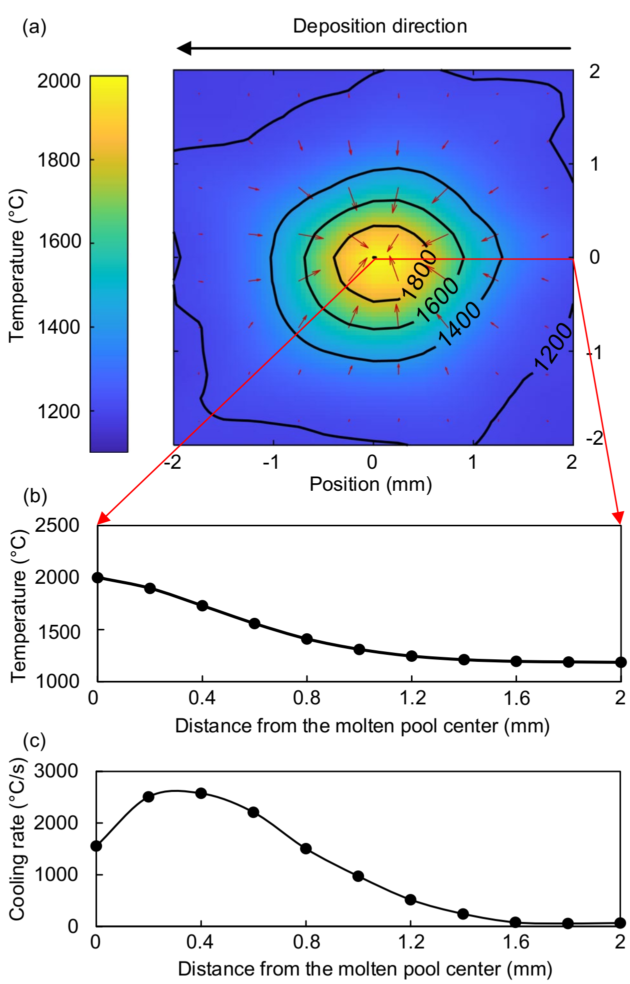

Fig. 4 Illustration on molten pool characterization including morphology, maximum temperature, and cooling rate

The thermal gradients were calculated and represented by the size and direction of the arrows. In single-track build experiments, the coatings were deposited in the x-direction. It is possible to derive the cooling rate in the x-direction by scaling these thermal gradients with the scanning speed (5 mm/s). The cooling rate CR in the x-direction during the deposition process can be calculated as Eq. 3.

$$CR = \frac{dT}{dx} \times \frac{dx}{dt} \tag{3}$$

where T is the temperature (°C), x is the distance (mm), and t is the time (s). The absolute value of the cooling rate in the x-direction is shown in Fig. 4(c). Along the direction away from the center of the molten pool, the cooling rate increased and then decreased. The highest cooling rate was found on the liquid side of the solid–liquid interface. It has been reported that the cooling rate around the solid–liquid interface had decisive effects on the microstructure morphologies, phases, and mechanical properties of the CoCrFeNiTi HEA coatings. Due to this reason, in this study, the maximum cooling rate during the deposition processes was utilized to analyze the effects of powder geometry and laser power on the cooling rate and the properties of the fabricated coatings.

3 Results and discussion

3.1 Thermal analysis

3.1.1 Effects on the maximum molten pool temperature

Figure 5 shows the effects of powder geometry and laser power on the molten pool temperature. Figure 5(b) and Fig. 5(c) show the variation of the molten pool temperature with time during the deposition of CoCrFeNiTi HEA coatings from spherical-shaped powders and irregular-shaped powders, respectively. Under the conditions of using spherical-shaped and irregular-shaped powders, the effects of laser power on the molten pool temperature were similar. With the increase of laser power from 250 to 300 W, the molten pool temperature was slightly increased. When the laser power increased to 350 W, the maximum molten pool temperature significantly increased by 18.5%. This nonlinear molten pool temperature increase could be explained by the changes in the molten pool size. As shown in Fig. 6, when the laser power increased from a relatively low level (from 250 to 300 W), the molten pool size was significantly increased. The larger molten pool size resulted in more feedstock powders being caught and melted by the molten pool, which suppressed the increase of molten pool temperature [28]. When the laser power increased from 300 to 350 W, the molten pool size had barely changed due to the limitation

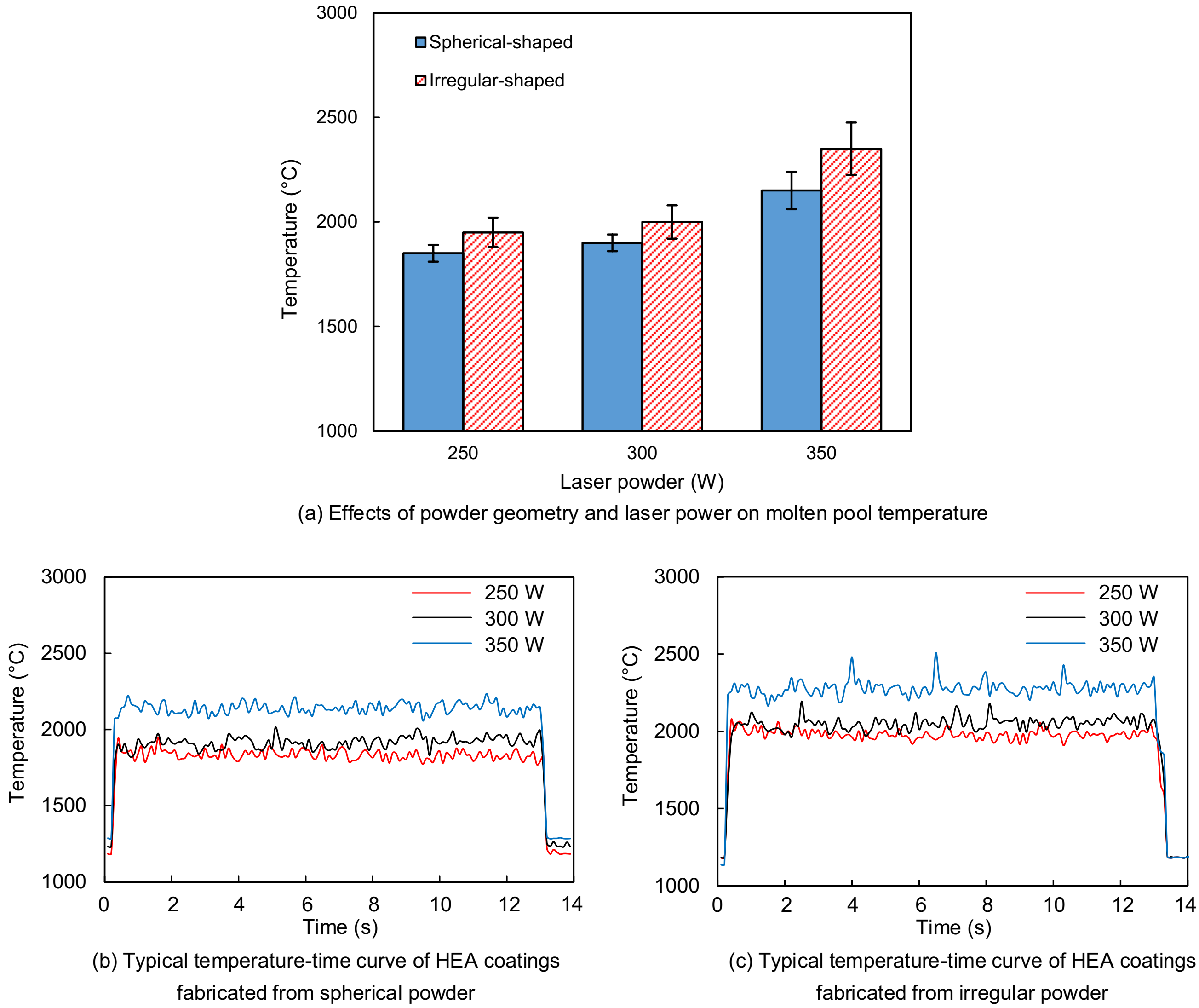

Fig. 5 Effects of powder geometry and laser power on the molten pool temperatures

of the laser spot size (400 μm). The molten pool would not absorb and melt more feedstock powders. A higher laser power could significantly increase the temperature of the liquids in the molten pool. A similar phenomenon had been reported by Hofmeister et al. and Jiang et al. [29, 30].

Under the same level of laser power, the molten pool temperature of the coatings fabricated from irregular-shaped powders was always higher than that of the coatings fabricated from spherical-shaped powders. The main reason for the variation in molten pool temperature was the different laser absorption rates of these two kinds of feedstock power. For the powder materials, the smaller powder size and irregular shape could reduce the gap between each powder particle, which increased the actual irradiation area. In addition, the smaller particle size caused most of the first reflected light to experience multiple reflections and scattering. The incident rays were more difficult to escape into the external environment. Due to the larger actual irradiation area and higher laser utilization rate, the irregular-shaped feedstock powder with a smaller particle size had a higher laser absorption rate. The similar phenomenon had been reported by Niu et al. and Zhang et al. [31, 32]. Under the same level of laser power, using irregular-shaped feedstock powders with a higher laser absorption rate could increase the actual energy density, leading to a higher molten pool temperature.

3.1.2 Effects on cooling rate

Figure 7 shows the effects of powder geometry and laser power on cooling rates of CoCrFeNiTi HEA coatings fabricated from spherical-shaped powders under different levels

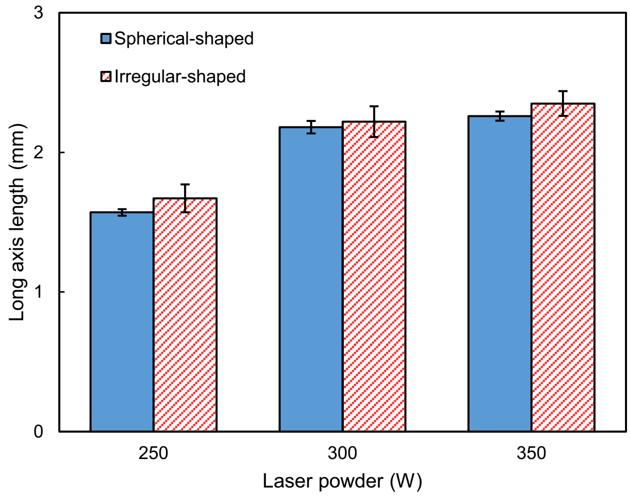

Fig. 6 Effects of powder geometry and laser power on the molten pool size (long axis length)

of laser power. Figure 7(b) and Fig. 7(c) show the variation of the cooling rate with time during the deposition of CoCrFeNiTi HEA coatings fabricated from spherical-shaped powders and irregular-shaped powders, respectively. For both coatings fabricated from spherical-shaped and irregular-shaped powders, when the laser power increased to 300 W, the cooling rate was significantly decreased. As discussed in Sect. 3.1.1, under a relatively low laser power, with the increase of laser power, the size of the molten pool was significantly increased. At the same time, the molten pool temperature was slightly increased. The larger molten pool size and similar molten pool temperature led to the decrease of the thermal gradient in the molten pool, resulting in a lower cooling rate [33]. With the laser power further increasing from 300 to 350 W, the cooling rate was slightly decreased. Under a high level of laser power, the area of the heat-affected zone was significantly increased. This resulted in a lower thermal gradient near the solid–liquid surface, which slightly reduced the cooling rate at the boundary of the molten pool.

Under the same level of laser power, the utilization of irregular-shaped powders could increase the temperature of the molten pool, but the cooling rate was not significantly decreased. The possible reason was that the powder absorption rate of the molten pool is sensitive to powder geometry. The irregular-shaped powders were hard to be caught by the melt pool and thus adhered to the substrates near the molten pool [34]. These high-temperature powders could increase the temperature of the substrate near the solid–liquid surface and thus reduce the cooling rate at the boundary of the molten pool. Since the effects of powder geometry on cooling rate reduction were complex, in the future, more experimental and theoretical studies are needed to further explain this phenomenon.

3.2 Effects on phase constitution

The XRD patterns of CoCrFeNiTi HEA coatings fabricated from spherical-shaped and irregular-shaped powders under different levels of laser power are shown in Fig. 8. The diffraction peaks with high intensity could be identified as the solid solution with an FCC lattice structure, while the remaining diffraction peaks with low intensity are matched with the Laves phase and X phase, which is similar to the investigations from Tadashi et al. [20].

According to the formula of interplanar distance for cubic crystals (Eq. 4) and the Bragg diffraction law (Eq. 5), the relationships between Bragg diffraction angles and lattice parameter (a) could be expressed by Eq. 6:

$$a = \frac{d}{\sqrt{h^2 + k^2 + l^2}} \tag{4}$$

$$d = \frac{n\lambda}{2sin\theta} \tag{5}$$

$$a = \frac{n\lambda\sqrt{h^2 + k^2 + l^2}}{2sin\theta} \tag{6}$$

where d is the interplanar distance, nm; θ is Bragg diffraction angle; λ is the diffracted wavelength (0.15406 nm); and h, k, and l are Miller index. With the increase of laser power, the peak locations (2θ) of the FCC solid solution phase in the fabricated coatings slightly shift toward the left. According to Eq. 5, the smaller Bragg diffraction angles θ of the FCC solid solution phase indicated that the increase of laser power could result in the increase of lattice parameter. The increase of lattice parameter could be attributed to the solid solution of Ti with a larger atomic radius in the FCC solid solution. As discussed in Sect. 3.1, the higher level of laser power could increase the molten pool temperature and decrease the cooling rate. The fluidity of the liquid materials was increased and the solidification time was prolonged, which enhanced the atomic migration ability and the solid solution of Ti.

When the laser power increased from 250 to 350 W, the intensity of the peaks representing Laves phase was increased. This increasing trend was similar to that of the molten pool temperature. The increase of molten pool temperature and decrease of cooling rate had a major impact on the prolongation of the solidification process. The element segregation was intensified, which promoted the precipitation of Laves phase [35]. In addition, with the increase of laser power, the content of X phase was slightly increased, which could also be attributed to the prolonged solidification process.

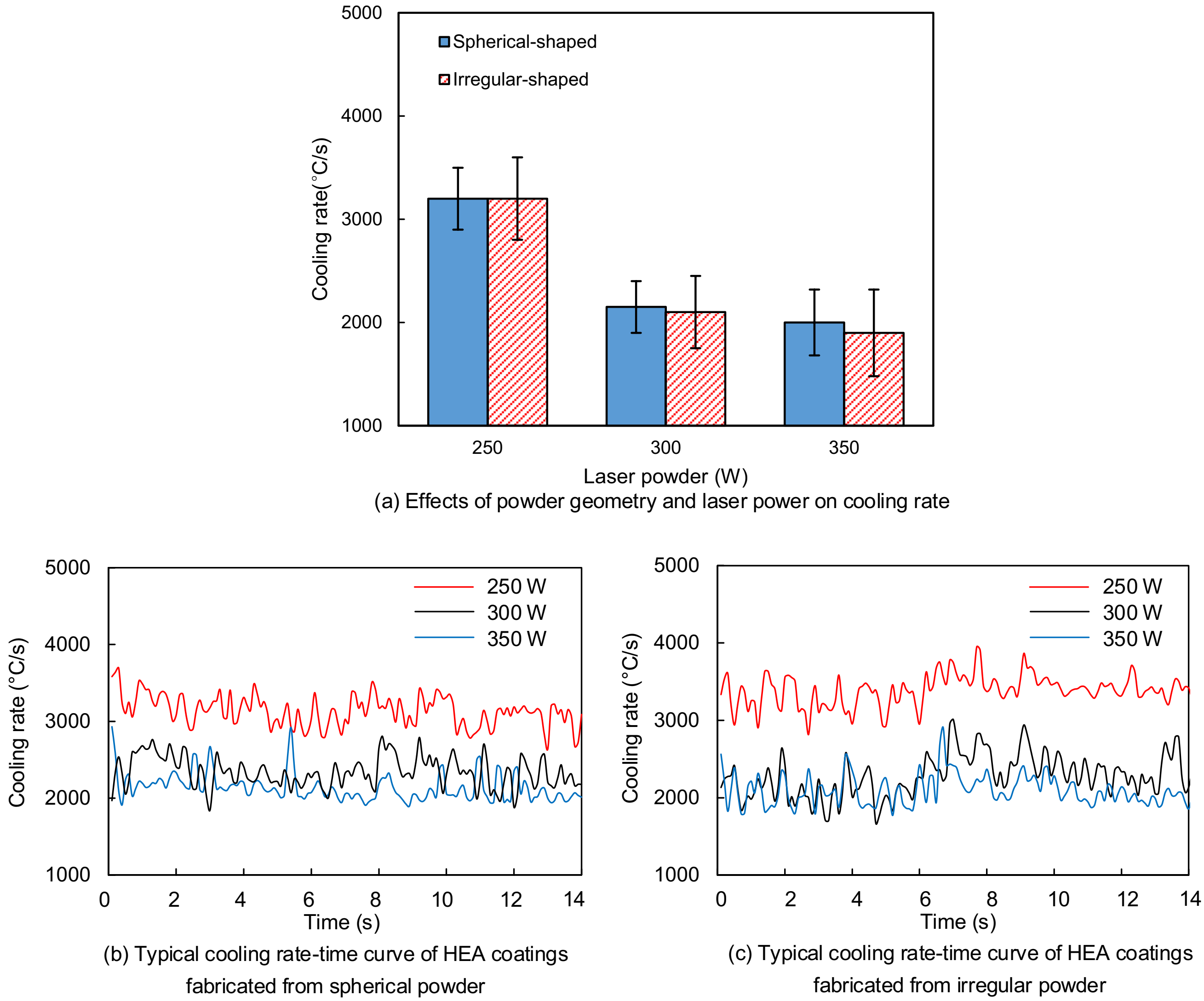

Fig. 7 Effects of powder geometry and laser power on the cooling rate

Under the same level of laser power, by using the irregular-shaped powders, the intensity of the peak representing Laves phase was increased, especially under the laser power of 250 W and 300 W. As discussed in Sect. 3.1.2, under the laser power of 250 W and 300 W, the molten pool temperature of the coatings fabricated from spherical-shaped powders was low (around 1850 to 1900 °C), which was close to the melting point of CoCrFeNiTi HEA (around 1780 °C). By using the irregular-shaped powders, the molten pool temperature and solidification time were significantly increased. In addition, powder shape had little effect on the cooling rate. Due to these two reasons, under a low level of laser power, the utilization of irregular-shaped power could significantly prolong the solidification time, which could effectively promote the formation of the precipitated Laves phase [36].

3.3 Effects on microstructure and element composition

Figure 9 and Fig. 10 show the effects of powder geometry and laser power on microstructure and element composition. Under the laser power of 250 W, the dark regions and a small amount of line-shaped light features were finely dispersed in the grey matrix. There were also some black spots distributed in the coatings, which were the micropores generated during the fabrication. The generation of micropores was mainly attributed to the interaction of laser beam, inert gas, and metal powders, the complex molten pool flow characteristics, and the change in material volume during the alloying process [37, 38]. Point 1, point 2, and point 3 were selected in dark regions, grey matrix, and white features, respectively. The element compositions of these three regions

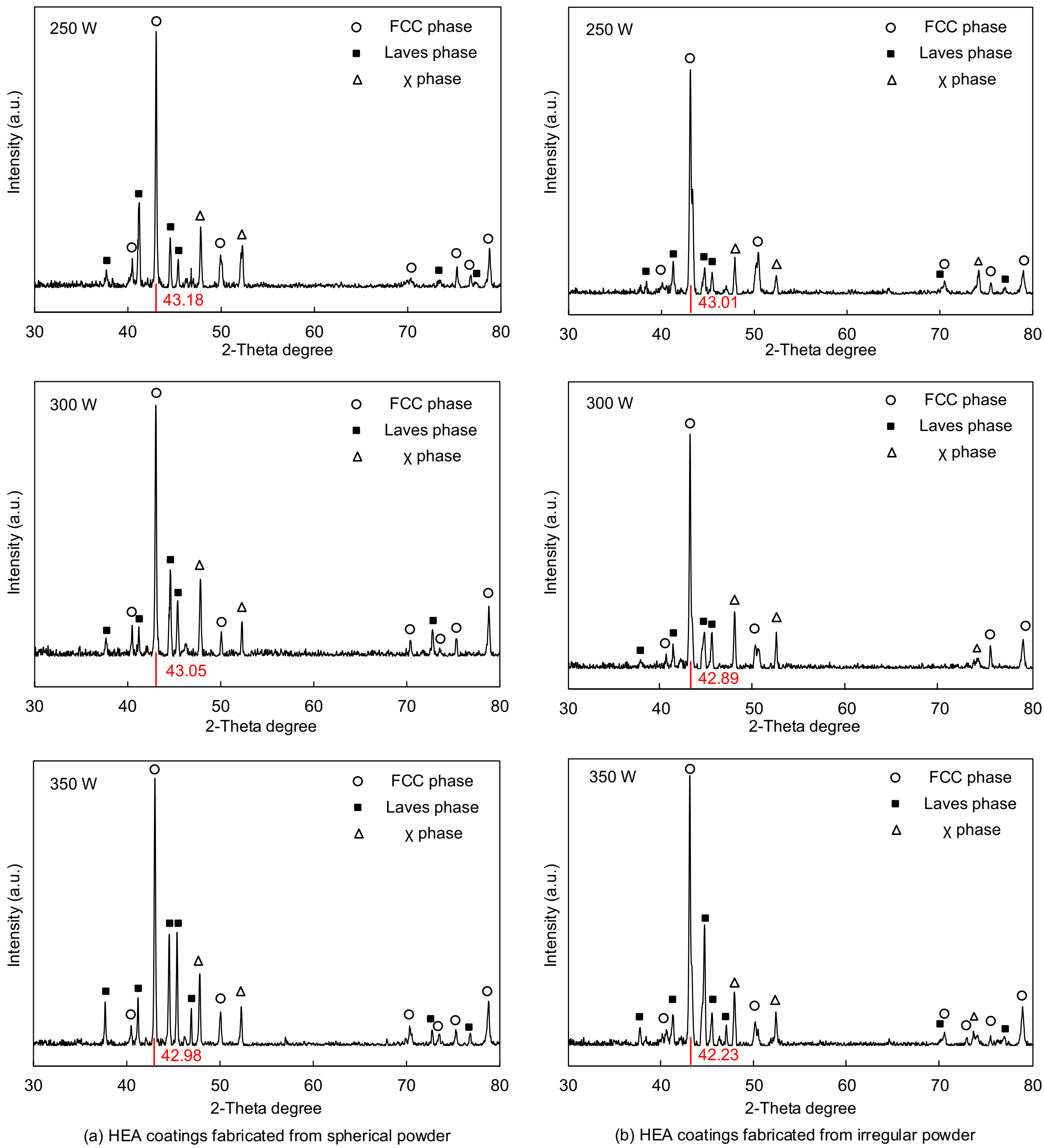

Fig. 8 Effects of powder geometry and laser power on the phase constitutions of CoCrFeNiTi HEA coatings

were shown in Fig. 10(a). The white features were rich in Ni, Ti, and Co with approximately similar amounts of Cr and Fe. For the elements that we used in this investigation, the mixing enthalpies between Ti and Co, Cr, Fe, and Ni were − 28, − 7, − 17, and − 35 kJ/mol, respectively [39]. The largest negative ΔH_{mix} of (Ti, Ni) and (Ti, Co) facilitated the formation of the precipitated (Ti, Ni)-rich X phase and (Ti, Co)-rich Laves phase during solidification, which had also been reported as Jiang et al. [19]. The dark regions were rich in Fe and Ti with approximately similar amounts of Co, Cr, and Ni, which were FCC solid solution phase. The formation mechanisms were that Ni and Co were enriched

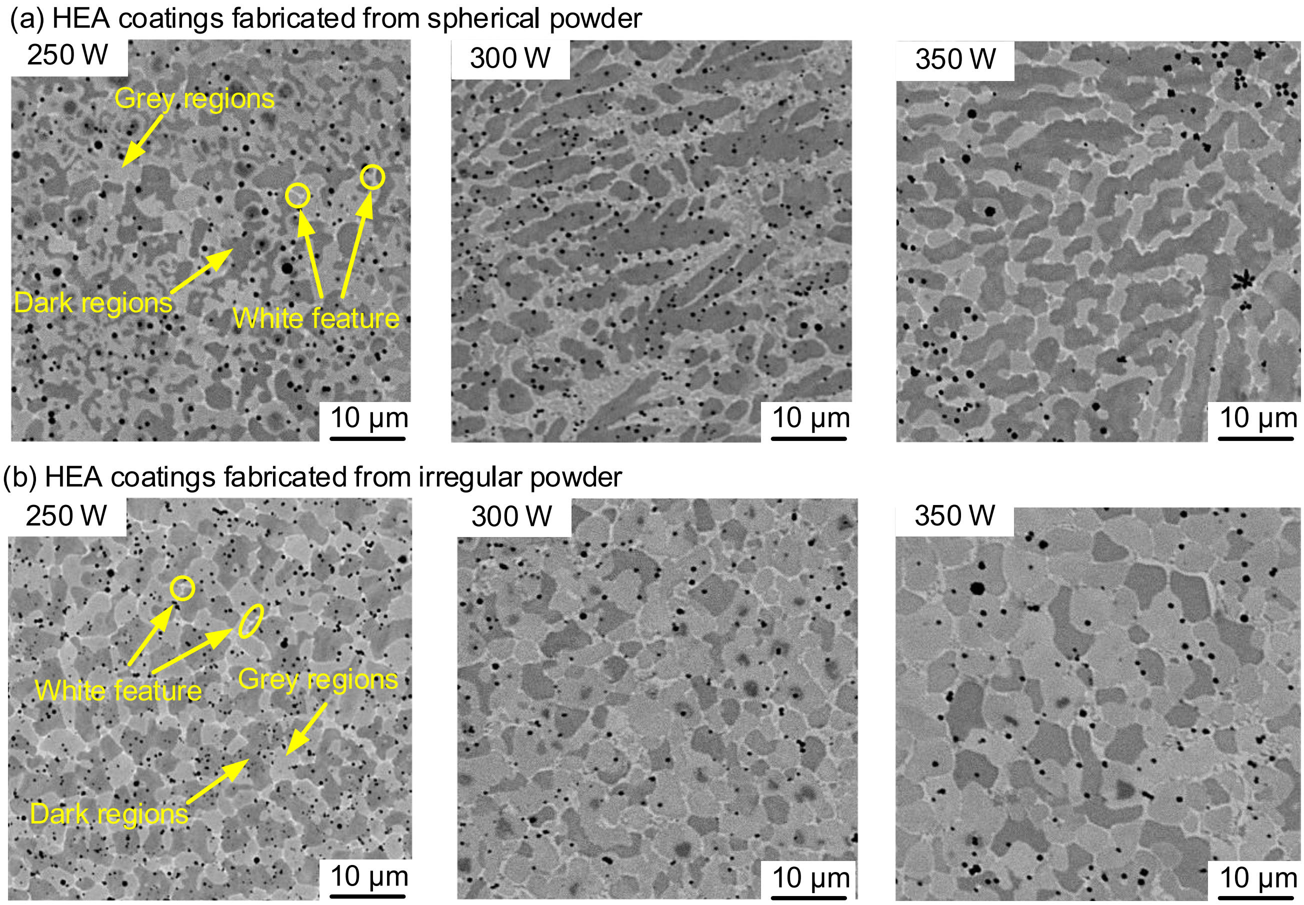

Fig. 9 Effects of powder geometry and laser power on microstructure morphologies of CoCrFeNiTi HEA coatings

in the X phase and the Laves phase, leading to the higher content of Cr and Fe in other regions. As discussed before, except for Ni and Co, Fe has the negative ΔH_{mix} with Ti. Therefore, Fe and Ti were rich in the dark region. The grey matrix had approximately similar amounts of Co, Cr, Fe, Ni, and Ti, which also were FCC solid solution phase. The high entropy effect at high temperatures reduces the Gibbs free energy of the solid solution phase, and the principle of the mixture is the obvious mechanism for HEAs [40]. When the laser power increased to 300 W and 350 W, the size of dark regions was significantly increased since the lower cooling rate and lower thermal gradient always led to larger grain size. In addition, it can be seen that with the increase of laser power, there were more Laves phase and X phase (light features) in the fabricated coatings, which was consistent with the phase analysis in Sect. 3.2. The reason was that the higher laser power could increase the molten pool temperature and prolong the solidification process, which promoted the occurrence of segregation and precipitation of X phase and Laves phase.

Figure 9(b) shows the microstructure of CoCrFeNiTi HEA coatings fabricated from irregular-shaped powders under different levels of laser power. The microstructure was also composed of three different regions: the dark regions, the grey matrix, and the light features. The size and the number of micropores were similar to those in the coatings fabricated with spherical-shaped powders. The element compositions of these three regions were shown in Fig. 10(b). It can be found that the element compositions of these three regions were similar to those in the coatings fabricated from spherical-shaped powders. The light features were Laves phase and X phase. The dark regions and grey matrix were FCC solid solution phase. Compared with Fig. 9(a) and Fig. 9(b), it could be found that when the coatings were fabricated from irregular-shaped powders under 300 W and 350 W laser power, the dark regions were changed from long strip shapes in different sizes to isometric shapes in similar sizes. In this study, the five kinds of metal powder used had different thermodynamic properties. When the coatings were fabricated from spherical-shaped powders, the high melting point Cr and Ti powders might be partially melted, resulting in the decrease in the fluidity of the liquid material within the molten pool. The temperature gradient distribution within the melt pool was uneven, resulting in

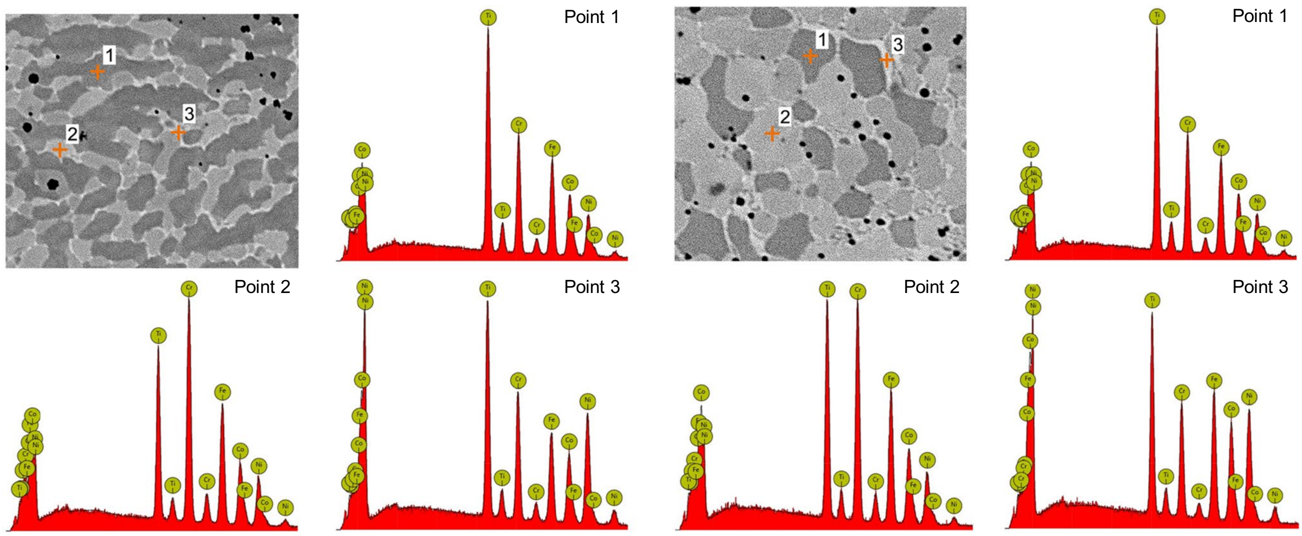

Element	Point 1 (at.%)	Point 2 (at.%)	Point 3 (at.%)
Ti	22.60	19.68	18.28
Fe	22.82	20.31	14.11
Co	20.43	19.59	18.75
Cr	18.31	20.85	15.41
Ni	15.84	19.57	33.45

(a) HEA coatings fabricated from spherical powder

Element	Point 1 (at.%)	Point 2 (at.%)	Point 3 (at.%)
Ti	22.77	20.95	18.71
Fe	20.88	20.87	15.82
Co	19.26	19.15	20.46
Cr	19.22	20.61	15.23
Ni	17.87	18.42	29.78

(b) HEA coatings fabricated from irregular powder

Fig. 10 Effects of powder geometry and laser power on element distributions of CoCrFeNiTi HEA coatings

the generation of long strips of grain with different sizes. As a comparison, the utilization of irregular-shaped powders could significantly increase the temperature of the melt pool. The fluidity of the liquids in the molten pool was improved and the temperature distribution was more uniform. In this case, the heat flux was ordered and vertical downward due to the good thermal conductivity of Ti substrates, resulting in the growth of grain in the horizontal direction [41]. Therefore, the grains had isometric shapes, and the microstructure became more uniform.

3.4 Effects on mechanical properties

3.4.1 Effects on microhardness

Figure 11 shows the effects of powder geometry and laser power on the microhardness of CoCrFeNiTi HEA coatings. As shown in Fig. 11(a), under the lase power of 250 W and 300 W, the microhardness of CoCrFeNiTi HEA coatings fabricated from the spherical-shaped powder was similar (~ 600 $HV_{1.0}$), which was almost three times higher than that of the Ti substrate (~ 210 $HV_{1.0}$). According to the Hall–Petch equation, $\sigma = \sigma_0 + kd^{(-1/2)}$, it could be inferred that a larger grain size could reduce the microhardness of the coatings. However, there was no significant decrease in microhardness. There were two reasons. First, as discussed in Sect. 3.2, with the increase of laser power, more Ti atoms were dissolved into the lattice of the FCC solid solution phase, leading to the promoted solid solution strengthening effects. Second, the higher laser power promoted the precipitation of Laves phase, which had extremely high hardness [23]. As the laser power increased to 350 W, the microhardness of the fabricated coatings reached 790 $HV_{1.0}$. The higher hardness was attributed to the large amount of high-hardness Laves phase. Figure 11(b) shows that the microhardness of the coatings fabricated by irregular-shaped powders was increased with increase of laser power. Although the higher laser power increased the grain size, the precipitation of the Laves phase is greatly facilitated, which had a major impact on the microhardness improvement.

Under the same level of laser power, the microhardness of the coatings fabricated from irregular-shaped powders was always higher than that fabricated by spherical-shaped powders. This phenomenon could also be explained by the Hall–Petch formula, solid solution strengthening, and precipitation of the Laves phase. As discussed in Sect. 3.3, the utilization of irregular-shaped powders resulted in a more uniform microstructure and a smaller grain size, which contributed to the improvement of the microhardness. Meanwhile, by comparing the elemental content data in Fig. 10(a) and Fig. 10(b), and the XRD data in Fig. 8(a) and Fig. 8(b), it could be found that under the same level of laser power,

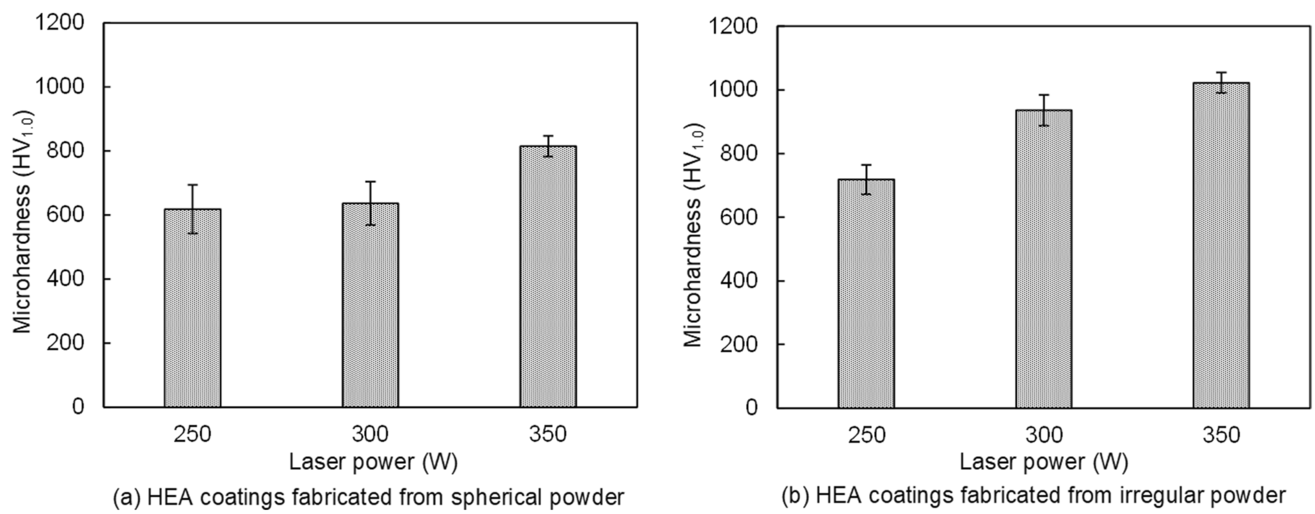

Fig. 11 Effects of powder geometry and laser power on microhardness of CoCrFeNiTi HEA coatings

the solid solution strengthening effects in the coatings fabricated from irregular-shaped powders was stronger and the precipitation of Laves phase was also promoted. The higher hardness of matrix with FCC phase and higher content of high-hardness Laves phase increased the hardness of the fabricated coatings.

In addition, the microhardness values CoCrFeNiTi HEA coatings/parts from this investigation and other existing investigations were compared, which were listed in Table 2. When CoCrFeNiTi coatings were fabricated using spherical-shaped powders, the highest microhardness of the CoCrFeNiTi HEA coatings (fabricated under 350 W laser power) in this study was 790 HV, which was similar to that in other studies [22, 23, 25]. The microhardness of CoCrFeNiTi HEA coatings/parts using spherical-shaped powders ranged from 568 to 830 HV. As a comparison, the microhardness of the HEA coatings using irregular-shaped powders ranged from 850 to 1010 HV, which was higher than that of the HEA coatings/parts fabricated using spherical powders [27, 42]. The microhardness results in this study was in trend agreement with those in other existing investigations, which further proved the accuracy of the findings and conclusions in this study.

3.4.2 Effects on wear resistance

Figure 12 shows the effects of powder geometry and laser power on the wear resistance of CoCrFeNiTi HEA coatings. The wear rates of the CoCrFeNiTi HEA coatings fabricated from spherical-shaped powders under different levels of laser power were shown in Fig. 12(a). The wear resistance was inversely correlated with wear rate. It could be seen that with the increase of laser power, the wear resistance was increased. To further investigate

Table 2 The input parameter and microhardness of CoCrFeNiTi HEA fabricated by laser additive manufacturing process

Alloy	Laser power (W)	Laser type	Powder shape	Powder size (μm)	Microhardness (HV)	Refs
CoCrFeNiTi	350	Fiber laser	Spherical	10–75	790	-
CoCrFeNiTi	350	Fiber laser	Spherical Co, Fe, Ni Irregular Cr, Ti	~45	1010	-
CoCrFeNiTi	1800	CO_2 laser	Spherical	45–150	700	[22]
CoCrFeNiTi	3000	CO_2 laser	Spherical	48–100	568	[23]
$CoCrFeNiTi_{0.3}$	1300	CO_2 laser	Spherical	~100	~400	[25]
$CoCrFeNiTi_{0.5}$	1300	CO_2 laser	Spherical	~100	~510	[25]
$CoCrFeNiTi_{0.7}$	1300	CO_2 laser	Spherical	~100	830	[25]
$Co_{25}Cr_{16.7}Fe_{16.7}Ni_{25}Ti_{16.7}$	350	Fiber laser	Spherical Co, Ni, Irregular Fe, Ti flake-shaped Cr	45–150	852.95	[26]
CoCrFeNiTi	300	Fiber laser	Spherical Co, Fe, Ni Irregular Cr, Ti	10–75	916 (after laser remelting)	[27]

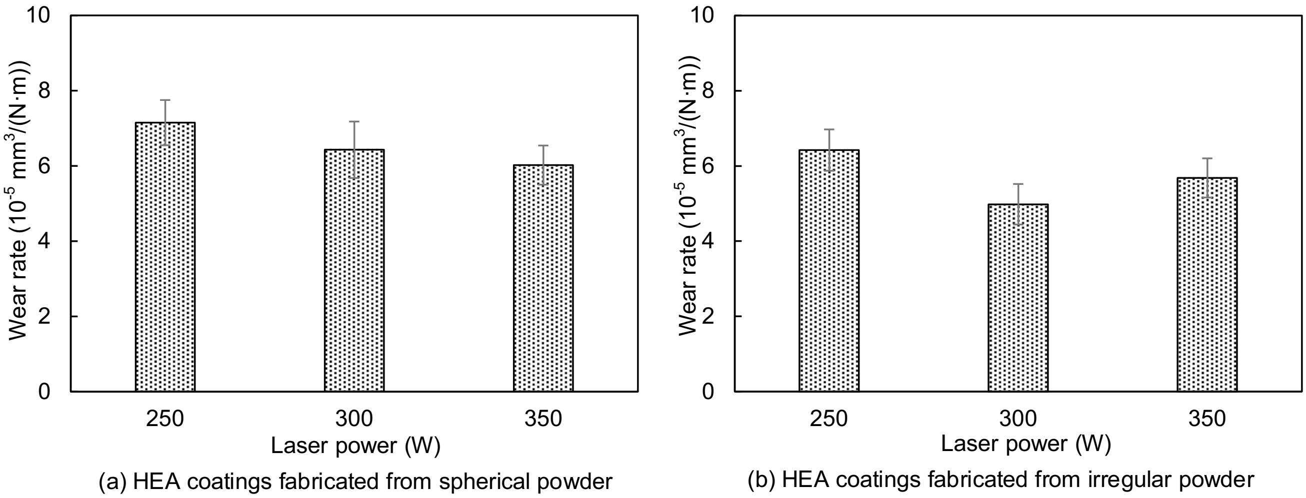

Fig. 12 Effects of powder geometry and laser power on wear rate of CoCrFeNiTi HEA coatings

the wear mechanism, the coefficient of friction and the SEM images of the worn surface was shown in Fig. 13(a) and Fig. 14(a), respectively. It could be seen that for the coatings that were fabricated with spherical powders, the level of laser power had little effects on coefficient of friction. In the SEM images, it could be found that with the increase of laser power, the morphologies of worn surfaces were barely changed, which indicates that the increase in laser power would not change the friction mechanism. The main reason for the increase in the wear resistance of the coatings was the increase in hardness. The higher microhardness meant that the coatings were more resistant to the SiC ball pressing into the surface during the dry sliding test. The lower indentation depth of SiC ball, the smaller wear volume lost was, which meant the higher wear resistance.

The wear rate, coefficient of friction, and worn surface of the coatings fabricated from irregular-shaped powders were shown in Fig. 12(b), Fig. 13(b), and Fig. 14(b), respectively. For the coatings that were fabricated with irregular powders, the increase in the laser power to 350 W resulted in a significant increase in fabrication of coefficient. The average friction coefficient of the coatings fabricated under 350 W laser power (~0.54) was higher than that of the coatings fabricated under 250 W and 300 W (~0.44 and 0.45). In order to better investigate the reasons for the variation of the friction coefficient, the surface morphology of the worn surface was obtained and analyzed. It can be seen that with the increase of laser power, there were more cracks and abrasive chips on the worn surface after dry sliding tests, which would increase the coefficient of friction. The wear mechanisms changed from adhesive wear to a combination

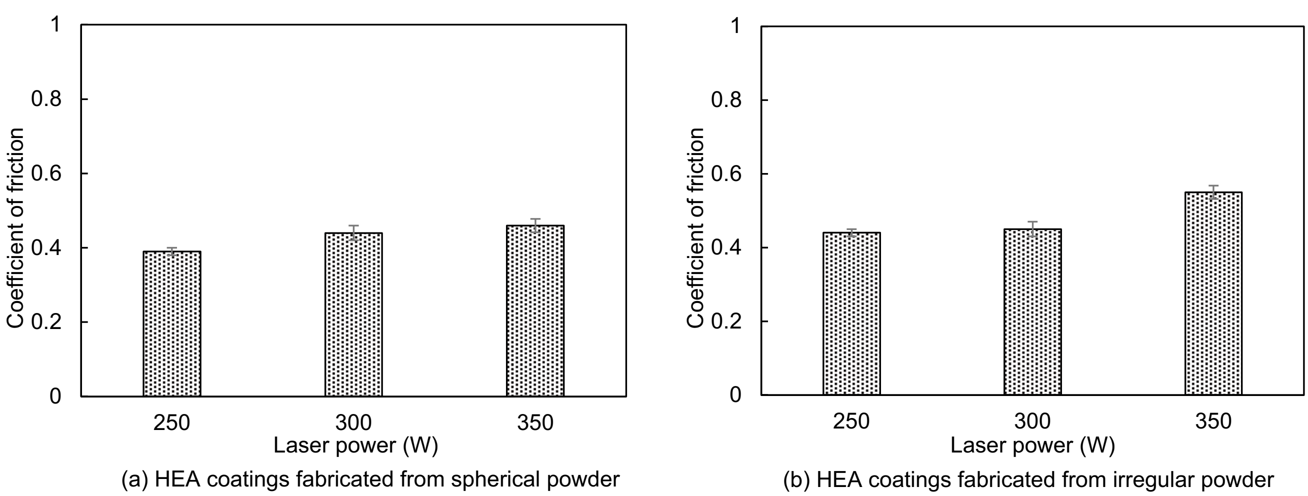

Fig. 13 Effects of powder geometry and laser power on friction coefficient of CoCrFeNiTi HEA coatings

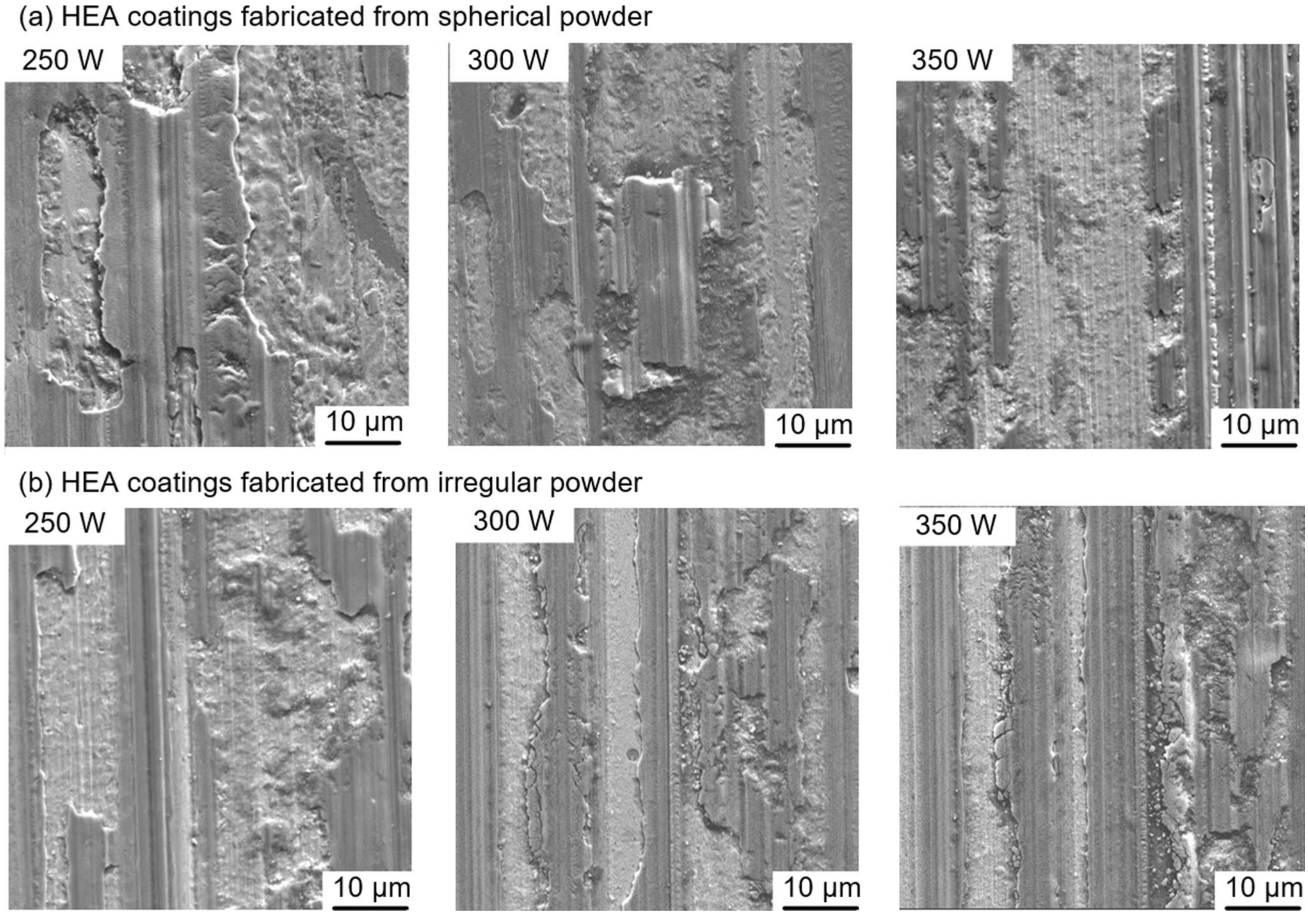

Fig. 14 Effects of powder geometry and laser power on worn surface after dry sliding tests

of abrasive wear and adhesive wear. The main reason for the change in the wear mechanism was that the coatings fabricated with irregular powders at high level of laser power had a higher content of Laves phase and X phase. These high-hardness and brittle phases would be separated from the FCC matrix during dry sliding tests. The micro-cracks produced during the separation process and the scraping effect of the separated abrasive chips inhibited the production of a smooth worn surface.

Under the 250 W and 300 W of laser power, the wear resistance of the coatings fabricated from irregular-shaped powders was higher than that fabricated by spherical-shaped powders. As discussed in Sect. 3.4.1, the microhardness of the coatings fabricated with irregular-shaped powders was higher than that fabricated with spherical-shaped powders due to the more uniform microstructure, the smaller grain size, and the higher content of hard phases. The higher microhardness meant the higher wear resistance. Under the 350 W of laser power, the wear resistance of the coatings fabricated from irregular-shaped powders was similar to that fabricated by spherical-shaped powders. The higher microhardness of the coatings fabricated with irregular powder could not improve the wear resistance. There were more high hardness abrasive chips generated during the dry sliding tests, which aggravated the material removal and thus reducing the wear resistance of the coating.

4 Conclusion

In this study, CoCrFeNiTi HEA coatings were fabricated by laser DED process using spherical-shaped and irregular-shaped powders. The effects of powder geometry and laser power on molten pool characterizations, phases, microstructure, element compositions, and mechanical properties of the deposited coatings have been investigated. The major conclusions are drawn as follows:

- The higher laser power could increase the molten pool temperature due to the higher energy density. Under the high level of laser power (350 W), the cooling rate was significantly decreased since the molten pool size was increased, which reduced the thermal gradient. The irregular-shaped powders could increase the molten pool temperature, which could be attributed to their higher laser absorption. Under the same level of laser power, the shape of powders had little influence on the cooling rate.

- With the increase of laser power, the solid solution strengthening of FCC solid solution phase and precipitation of Laves phase was promoted. The grain size was increased due to the lower cooling rate. By using irregular-shaped powders, the microstructure became more uniform since the higher molten pool temperature uniformed the thermal gradient.
- Using higher laser power and irregular-shaped powders could increase the microhardness. This could be attributed to the solid solution strengthening of the FCC solid solution phase and the promoted precipitation of Laves phase with high hardness.
- With the increase of laser power, the wear resistance of the coatings fabricated by spherical-shaped powders was increased due to the increase of hardness. The wear resistance of the coatings fabricated by irregular-shaped powders was increased and then decreased due to the formation of cracks and abrasive chips from brittle phases. Under 300 W, the coatings fabricated by irregular-shaped powders had the best wear resistance.

Author contribution Yunze Li: methodology, investigation, validation, writing—original draft. Dongzhe Zhang: investigation, writing—review and editing. Yingbin Hu: writing—review and editing. Weilong Cong: writing—review and editing.

Data availability The data supporting the conclusions are included in the article.

Declarations

Ethics approval The authors confirm that they have abided by the publication ethics and state that this work is original and has not been used for publication anywhere before.

Consent to participate The authors are willing to participate in journal promotions and updates.

Consent for publication The authors give consent to the journal regarding the publication of this work.

Conflict of interest The authors declare no competing interests.

References

1. Harea E, Stoček R, and Machovský M (2017) Study of friction and wear of thermoplastic vulcanizates: the correlation with abraded surfaces topology. J Phys Conf Ser. 843:012070. IOP Publishing
2. Tsai M-H, Yeh J-W (2014) High-entropy alloys: a critical review. Mater Res Lett 2(3):107–123
3. Guo S, Ng C, Lu J, Liu C (2011) Effect of valence electron concentration on stability of fcc or bcc phase in high entropy alloys. J Appl Phys 109(10):103505
4. Yeh JW, Chen YL, Lin SJ, Chen SK (2007) High-entropy alloys–a new era of exploitation. Mater Sci Forum 560:1–9 (Trans Tech Publ)
5. Zhang, Y (2019) High-Entropy Materials. Springer Nat Singap Pte Ltd 2:215–232
6. Gwalani B, Ayyagari AV, Choudhuri D, Scharf T, Mukherjee S, Gibson M, Banerjee R (2018) Microstructure and wear resistance of an intermetallic-based $Al_{0.25}Ti_{0.75}CoCrFeNi$ high entropy alloy. Mater Chem Phys 210:197–206
7. Haftlang F, Zargaran A, Son S, Lee S, Hong S-J, Kim HS (2022) The subsurface deformed region and superficial protective tribo-oxide layer during wear in a non-equiatomic CoCrFeNiV high entropy alloy. Mater Des 218:110685
8. Fang S, Chen W, Fu Z (2014) Microstructure and mechanical properties of twinned $Al_{0.5}CrFeNiCo_{0.3}C_{0.2}$ high entropy alloy processed by mechanical alloying and spark plasma sintering. Mater Des 54:973–979
9. Fu Z, Chen W, Fang S, Zhang D, Xiao H, Zhu D (2013) Alloying behavior and deformation twinning in a $CoNiFeCrAl_{0.6}Ti_{0.4}$ high entropy alloy processed by spark plasma sintering. J Alloy Compd 553:316–323
10. Zhang P, Li Y, Chen Z, Zhang J, Shen B (2019) Oxidation response of a vacuum arc melted NbZrTiCrAl refractory high entropy alloy at 800–1200 C. Vacuum 162:20–27
11. Liu Y, Wang G, Zhao Y, Wang M, He R, Tan C, ... Zhou X (2021) Joining of SiC using CoFeCrNiCuTi high entropy alloy filler by electric current field assisted sintering. J Eur Ceramic Soc 42(5):1995–2003
12. Wang R, Zhang K, Davies C, Wu X (2017) Evolution of microstructure, mechanical and corrosion properties of AlCoCrFeNi high-entropy alloy prepared by direct laser fabrication. J Alloy Compd 694:971–981
13. Yin S, Li W, Song B, Yan X, Kuang M, Xu Y, ... Lupoi R (2019) Deposition of FeCoNiCrMn high entropy alloy (HEA) coating via cold spraying. J Mater Sci Technol 35(6):1003–1007
14. Kgoete F, Popoola A, Fayomi O (2018) Influence of spark plasma sintering on microstructure and corrosion behaviour of Ti-6Al-4V alloy reinforced with micron-sized Si_3N_4 powder. Defence Technol 14(5):403–407
15. Sriharitha R, Murty B, Kottada RS (2014) Alloying, thermal stability and strengthening in spark plasma sintered AlxCoCrCuFeNi high entropy alloys. J Alloy Compd 583:419–426
16. Karthikeyan J (2007) The advantages and disadvantages of the cold spray coating process. In The cold spray materials deposition process, Woodhead Publishing. p 62–71
17. Agarwala M, Bourell D, Beaman J, Marcus H, Barlow J (1995) Direct selective laser sintering of metals. Rapid Prototyp J 1:26
18. Hu Y, Wang H, and Cong W (2019) Laser deposition-additive manufacturing of graphene oxide reinforced IN718 alloys: effects on surface quality, microstructure, and mechanical properties. Int Manuf Sci Eng Conf Am Soc Mech Eng 58752:V002T003A050
19. Jiang L, Lu Y, Dong Y, Wang T, Cao Z, Li T (2014) Annealing effects on the microstructure and properties of bulk high-entropy $CoCrFeNiTi_{0.5}$ alloy casting ingot. Intermetallics 44:37–43
20. Fujieda T, Chen M, Shiratori H, Kuwabara K, Yamanaka K, Koizumi Y, ... Watanabe S (2019) Mechanical and corrosion properties of CoCrFeNiTi-based high-entropy alloy additive manufactured using selective laser melting. Addit Manuf 25:412–420
21. Fujieda T, Shiratori H, Kuwabara K, Hirota M, Kato T, Yamanaka K, ... Watanabe S (2017) CoCrFeNiTi-based high-entropy alloy with superior tensile strength and corrosion resistance achieved by a combination of additive manufacturing using selective electron beam melting and solution treatment. Mater Lett 189:148–151

22. Liu H, Gao W, Liu J, Du X, Li X, Yang H (2020) Microstructure and properties of CoCrFeNiTi high-entropy alloy coating fabricated by laser cladding. J Mater Eng Perform 29(11):7170–7178
23. Zhang S, Han B, Li M, Zhang Q, Hu C, Niu S, ... Wang Y (2021) Investigation on solid particles erosion resistance of laser cladded CoCrFeNiTi high entropy alloy coating. Intermetallics 131:107111
24. Shun T-T, Chang L-Y, Shiu M-H (2012) Microstructures and mechanical properties of multiprincipal component CoCrFeNiTix alloys. Mater Sci Eng: A 556:170–174
25. Wang X, Liu Q, Huang Y, Xie L, Xu Q, Zhao T (2020) Effect of Ti content on the microstructure and corrosion resistance of CoCrFeNiTix high entropy alloys prepared by laser cladding. Materials 13(10):2209
26. Liu S, Grohol CM, Shin YC (2022) High throughput synthesis of CoCrFeNiTi high entropy alloys via directed energy deposition. J Alloys Compds 916:165469
27. Li Y, Hu Y, Zhang D, Cong W (2023) Laser remelting of CoCrFeNiTi high entropy alloy coatings fabricated by directed energy deposition: effects of remelting laser power. Opt Laser Technol 158:108871
28. Wang L, Felicelli S, Gooroochurn Y, Wang P, Horstemeyer M (2008) Optimization of the LENS® process for steady molten pool size. Mater Sci Eng: A 474(1–2):148–156
29. Hofmeister W, Wert M, Smugeresky J, Philliber JA, Griffith M, Ensz M (1999) Investigating solidification with the laser-engineered net shaping (LENSTM) process. Jom 51(7):1–6
30. Jiang Y, Cheng Y, Zhang X, Yang J, Yang X, Cheng Z (2020) Simulation and experimental investigations on the effect of Marangoni convection on thermal field during laser cladding process. Optik 203:164044
31. Zhang J, Gu D, Yang Y, Zhang H, Chen H, Dai D, Lin K (2019) Influence of particle size on laser absorption and scanning track formation mechanisms of pure tungsten powder during selective laser melting. Engineering 5(4):736–745
32. Niu H, Chang I (1999) Selective laser sintering of gas and water atomized high speed steel powders. Scr Mater 41(1):25–30
33. Farshidianfar MH, Khajepour A, Gerlich AP (2016) Effect of real-time cooling rate on microstructure in laser additive manufacturing. J Mater Process Technol 231:468–478
34. Wirth F, Freihse S, Eisenbarth D, and Wegener K (2017) Interaction of powder jet and laser beam in blown powder laser deposition processes: measurement and simulation methods. In Lasers in Manufacturing Conference, Munich, Germany, p 1–10
35. Chen J, Niu P, Liu Y, Lu Y, Wang X, Peng Y, Liu J (2016) Effect of Zr content on microstructure and mechanical properties of AlCoCrFeNi high entropy alloy. Mater Des 94:39–44
36. Radhakrishna C, Rao KP (1997) The formation and control of Laves phase in superalloy 718 welds. J Mater Sci 32(8):1977–1984
37. Zeng C, Tian W, Liao WH, Hua L (2016) Microstructure and porosity evaluation in laser-cladding deposited Ni-based coatings. Surf Coatings Technol 294:122–130
38. Geng Y, Konovalov S, Chen X (2020) Research status and application of the high-entropy and traditional alloys fabricated via the laser cladding. Usp Fiz Met 21:26–45
39. Takeuchi A, Inoue A (2005) Classification of bulk metallic glasses by atomic size difference, heat of mixing and period of constituent elements and its application to characterization of the main alloying element. Mater Trans 46(12):2817–2829
40. Middleburgh S, King D, Lumpkin G, Cortie M, Edwards L (2014) Segregation and migration of species in the CrCoFeNi high entropy alloy. J Alloy Compd 599:179–182
41. Zhou Y, Chen S, Chen X, Cui T, Liang J, Liu C (2019) The evolution of bainite and mechanical properties of direct laser deposition 12CrNi2 alloy steel at different laser power. Mater Sci Eng: A 742:150–161
42. Liu H, Gao Q, Dai J, Chen P, Gao W, Hao J, Yang H (2022) Microstructure and high-temperature wear behavior of $CoCrFeNiW_x$ high-entropy alloy coatings fabricated by laser cladding. Tribol Int 172:107574

Publisher's note Springer Nature remains neutral with regard to jurisdictional claims in published maps and institutional affiliations.